Time-dependent particle migration and margination in the pressure-driven channel flow of blood

Qin M. Qi* and Eric S. G. Shaqfeh†
Chemical Engineering, Stanford University, Stanford, California 94305, USA

(Received 14 September 2017; published 7 March 2018)

We present a theory to describe the time evolution of the red blood cell (RBC) and platelet concentration distributions in pressure-driven flow through a straight channel. This model is based on our previous theory for the steady-state distributions [Qi and Shaqfeh, Phys. Rev. Fluids **2**, 093102 (2017)] and captures the flow-induced nonuniformity of the concentrations of RBCs and platelets in the cross-flow direction. Starting with a uniform concentration, RBCs migrate away from the channel walls due to a shear-induced lift force and eventually reach steady state due to shear-induced diffusion, i.e., hydrodynamic "collisions" with other RBCs. On the other hand, platelets exit the cell-laden region due to RBC-platelet interactions and enter the cell-free layer, resulting in margination. To validate the theory, we also perform boundary integral simulations of blood flow in microchannels and directly compare various measureables between theory and simulation. The timescales associated with RBC migration and platelet margination are discussed in the context of the simulation and theory, and their importance in the function of microfluidic devices as well as the vascular network are elucidated. Due to the varying shear rate in pressure-driven flow and the wall-induced RBC lift, we report a separation of timescales for the transport in the near-wall region and in the bulk region. We also relate the transient problem to the axial variation of migration and margination, and we demonstrate how the relevant timescales can be used to predict corresponding entrance lengths. Our theory can serve as a fast and convenient alternative to large-scale simulations of these phenomena.

DOI: 10.1103/PhysRevFluids.3.034302

I. INTRODUCTION

The phenomena of red blood cell (RBC) migration and platelet margination have been studied extensively using experiments [1–4] and simulations [5–10]. There exists a consensus that in channel flow, RBCs migrate away from the walls due to their deformability that generates "lift." The resulting cell-free layer near the wall therefore is void of RBCs but has an excess concentration of platelets due to their hydrodynamic collisions with RBCs—i.e., "shear-induced diffusion." In the vascular system, migration and margination play a significant role in hemostasis [11] and thrombosis [12]. In *ex vivo* environments, these two phenomena have also been utilized in various microfluidic designs for applications such as cell sorting [13–16].

Despite the abundance of literature discussing particle migration and margination phenomena, few have investigated the evolution of these two cross-flow motions. The system is often assumed to be at steady state when measurements are taken. Nevertheless, the dynamics of particle migration and margination manifest themselves in two ways: the axial variation and the temporal variation. The axial variation is usually measured experimentally in terms of an entrance length parameter. Fitzgibbon

*qinq@stanford.edu
†Also at Mechanical Engineering, Stanford University, and Institute for Computational and Mathematical Engineering, Stanford University; esgs@stanford.edu

et al. [4] measured the distribution of platelet-sized microspheres in the cross-flow direction in a 30-μm channel with 1000 s^{-1} wall shear rate at distances of 1 to 3 cm downstream from a well-mixed reservoir. At 10% to 20% hematocrit (RBC volume fraction), these researchers estimated the entrance length for particle margination to be O(1 cm), i.e., much longer than the length scale for branching in the vascular network [17]. Another experimental observation was made by Carboni and Ma [18]. Based on tracking rigid particles 0.53 to 2.11 μm in diameter, they estimated the entrance length to be roughly 2.44 mm for the cell-free layer formation in a 40-μm channel with wall shear rates under 200 s^{-1}. Most simulation studies, however, consider the time-dependent problem with periodic boundary conditions at the inlet and outlet of simulation boxes. This transient problem is generally related to the entrance length problem by multiplying the time to steady state with the average flow velocity, but the validity of this approximation has yet to be examined. Katanov *et al.* simulated blood flow in 10–100 μm (D) tubes with a wide range of flow rates and reported an estimate of $25D$ for the cell-free layer entrance length, independent of shear rate [10]. Crowl and Fogelson [19] considered the time dependence of both platelet margination and RBC migration in their two-dimensional simulations. They proposed a drift-diffusion model to qualitatively capture these two phenomena. Effects of the initial concentration profile, hematocrit, and flow rates were investigated. However, as later pointed out by Zhao and coworkers [5], the value of the platelet diffusivity in two-dimensional simulations is largely underestimated and therefore the entrance length estimation made by Crowl and Fogelson may be inaccurate. Note that the entrance length estimate is an important design parameter for microfluidic applications. Even though the height of microfluidic channels may be O(10 μm), all estimates suggest that the length of the channel needs to be three orders of magnitude larger to allow complete migration and margination. If complex channel geometries, e.g., nonstraight channels, are used [15], additional considerations are necessary for the entrance length estimation to achieve optimal performance for purposes such as cell separation.

In our previous publication [20], we presented a coarse-grained theory that was used to predict RBC and platelet concentration distributions in the cross-stream direction at steady state in channel flow. We verified this theory against various simulations and experiments in terms of both the cell-free layer thickness and the concentration profile across the channel. Our work produced qualitative to semiquantitative results for a cellular suspension in pressure-driven flow. Compared to whole blood simulations, this theory requires much less computational power and is more flexible in handling rigid microparticles, such as platelets, at given hematocrit levels due to the decoupling of the RBC transport equation.

In this paper, we extend our theory to consider the time-dependence of RBC migration and platelet margination. We perform a systematic study of the effects of channel height, hematocrit, and the capillary number on the time evolution, and we examine the characteristics of the transient concentration distribution profile. Finally, we present a scaling analysis for the characteristic timescales in migration and margination. We demonstrate that both migration and margination are two-step processes with different governing mechanisms in the near-wall region, i.e., the cell-free layer, and the bulk region, i.e., the cell-laden region. Such a separation of timescales is partially due to the varying shear rate in a pressure-driven flow and is therefore less evident in a simple shear flow. Finally, we briefly discuss the axial variation of RBC migration and demonstrate that the actual entrance lengths are similar in magnitude to those approximated by the time-dependent problem. Our methodology can be adapted to other multicomponent systems consisting of particles with varying deformability and concentration and thus may have broader applications.

II. MODEL DESCRIPTION

A. Overview

In our previous work, we discussed in detail the approach to determining the governing fluxes in the cross-stream direction for both RBCs and platelets [20]. In this section, we briefly revisit the theory and highlight the differences in solving the time-dependent equations. We consider the

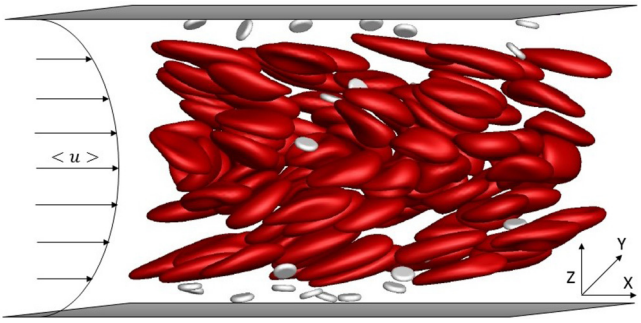

FIG. 1. A schematic of RBCs (red) and platelets (white) in wall-bound channel flow driven by a pressure gradient.

pressure-driven flow of blood through rectangular channels as shown in Fig. 1. We denote x as the flow direction, y as the vorticity direction, and z as the direction of the velocity gradient. We assume the y dimension is unbounded and thus ignore any variations in this direction. We solve for the number densities of RBCs n_C and platelets n_P as functions of both z and t.

We have summarized all the key parameter values in Table I below. RBCs and platelets are suspended in plasma, which is considered a Newtonian fluid with viscosity μ. We treat RBCs as deformable particles with a reduced volume v of 0.65 ($v = \frac{3\sqrt{4\pi}V}{S^{3/2}}$, V and S are RBC volume and surface area, respectively) and an equivalent RBC radius a ($\frac{4\pi a^3}{3} = V$). They have biconcave shapes at rest [21,22]. We model RBCs using the Skalak law [23] with shear modulus E_S, bending modulus E_B, and dilatational modulus E_D. Thus, the RBC membrane is nearly incompressible, has a characteristic resistance to shear, and a weak bending resistance. The ratio of internal to external fluid viscosity is kept at unity. Platelets are modeled as rigid oblate spheroids with the long axis being a_P and the shorter dimension being $1/4\, a_P$.

We choose the RBC radius a as our characteristic length scale. The characteristic shear rate $\dot{\gamma}_c$ is defined as the equivalent wall shear rate in parabolic flow corresponding to the average flow velocity $\langle u \rangle$ imposed. The inverse of $\dot{\gamma}_c$ is our characteristic timescale. In the limit of zero hematocrit, $\dot{\gamma}_c$ is equal to the actual wall shear rate $\dot{\gamma}_w$. We nondimensionalize all stresses by $\mu\dot{\gamma}_c$. The channel height L_z and the characteristic shear rate $\dot{\gamma}_c$ are chosen to match arteriole flow conditions [24]. Unless noted otherwise, all equations and results will be presented in dimensionless form.

The Reynolds number is assumed to be zero. Brownian motion is ignored for both RBCs and platelets due to their micron-size scales. With $\mathrm{Re} \to 0$ and $\mathrm{Pe} \to \infty$, the most significant

TABLE I. Summary of key parameter values used in theory and simulations.

a	Scaled units	Physical units
a	1	2.82 μm
a_P	0.5	1.41 μm
L_x	32	90.24 μm
L_y	9	25.38 μm
L_z	12, 17.73	33.84 μm, 50 μm
μ	1	1.2 cP
$\dot{\gamma}_C$	1	1000–2000 s^{-1}
E_S	2000 $\mathrm{s}^{-1}/\dot{\gamma}_C$	6.8 μN/m
E_D	100 $\mu\dot{\gamma}_C a$	
E_B	$3.3 * 10^{-3} a^2 E_S$	

TABLE II. Fitted values of lift velocity parameters from single cell simulations.

L_z	Ca	ξ	α
12	0.25	0.055	1.3
12	0.5	0.057	1.0
12	1	0.069	1.3
12	2	0.087	1.6
17.73	0.25	0.045	1.2
17.73	0.5	0.031	1.3
17.73	1	0.039	1.2
17.73	2	0.048	1.2
Vesicle experiments [25]		0.012 ± 0.002	1 ± 0.1

dimensionless parameter for our problem is the capillary number: $\mathrm{Ca} = \frac{\mu \dot{\gamma}_c a}{E_s}$. It represents the ratio of flow viscous effects to the mechanical forces resisting cell deformability. Based on the characteristics of RBCs, E_s denotes the membrane shear modulus. When the capillary number is unity, the corresponding $\dot{\gamma}_c$ is 2000 s^{-1}. We consider deformability-induced lift and shear-induced diffusion as governing mechanisms for the cross-flow transport of RBCs. Due to the relative paucity and rigidity of platelets, the platelet distribution is determined by the shear-induced diffusion created by RBC-platelet interactions and weak platelet-platelet interactions. Including only the major flux contributions, we write the governing equations for n_C and n_P in the form of advection-diffusion equations as follows:

$$\frac{\partial n_C}{\partial t} + \frac{\partial (u_{\mathrm{lift}} n_C)}{\partial z} + \frac{\partial F_{CC}}{\partial z} - \frac{\partial}{\partial z}\left(D \frac{\partial n_C}{\partial z} \right) = 0, \tag{1}$$

$$\frac{\partial n_P}{\partial t} + \frac{\partial F_{CP}}{\partial z} + \frac{\partial F_{PP}}{\partial z} = 0. \tag{2}$$

u_{lift} is the lift velocity of RBCs and was previously determined from boundary integral simulations [20]. Thus, we previously simulated single RBCs initially placed close to the wall and examined their motion as they underwent a cross-stream "lift" away from the wall until reaching the equilibrium position at the centerline of the channel. The calculated u_{lift} is then fit to the correlation: $u_{\mathrm{lift}} = \frac{\xi \dot{\gamma}_0(z)}{z^\alpha}$, where $\dot{\gamma}_0(z)$ denotes the dimensionless local shear rate. The coefficients ξ and α are tabulated below in Table II for various capillary numbers and channel heights.

F_{CC}, F_{CP}, and F_{PP} in Eqs. (1) and (2) denote fluxes created by RBC-RBC collisions, RBC-platelet collisions, and platelet-platelet collisions, respectively. We model these pair-wise collisions as Markovian processes [26] and the resulting fluxes can be written in a Boltzmann-like form:

$$F_{CC} = \int_{\delta_z} \int_{\delta_y} \int_0^{\Delta_{CC}} n_C(z-b) n_C(z-b-\delta_z) \delta u \, db \, d\delta_y \, d\delta_z, \tag{3a}$$

$$F_{PP} = \int_{\delta_z} \int_{\delta_y} \int_0^{\Delta_{PP}} n_P(z-b) n_P(z-b-\delta_z) \delta u \, db \, d\delta_y \, d\delta_z, \tag{3b}$$

$$F_{CP} = \int_{\delta_z} \int_{\delta_y} \int_0^{\Delta_{CP}} n_P(z-b) n_C(z-b-\delta_z) \delta u \, db \, d\delta_y \, d\delta_z. \tag{3c}$$

In the above expressions, δ_y and δ_z are the initial separation distances between two particles in the y and z directions. We impose a cutoff distance R of 3 cell radii on these interactions as the upper limit on δ_y and δ_z, as discussed in our previous work [20]. Hydrodynamic interactions between two particles result in asymmetric cross-flow displacement: Δ_{CC}, Δ_{PP}, and Δ_{CP}. We define these displacements with respect to the second particle and they are functions of z, y, and δ_z. We reference Δ_{CC}, Δ_{PP}, and Δ_{CP} values from our previous steady-state study [20]. To address the singularity

TABLE III. Best-fit D values based on the cell-free layer thickness at steady state.

L_z	Ht	D
12	10%	0.06
12	20%	0.14
12	30%	0.21
17.73	10%	0.07
17.73	20%	0.18
17.73	30%	0.27

issue at the centerline due to the vanishing shear rate, we add a nonlocal shear rate correction term ϵ to the local "center-of-mass shear rate" $\dot{\gamma}_0(z)$: $\dot{\gamma}(z) = \dot{\gamma}_0(z) + \epsilon\dot{\gamma}_c/2$, where $\epsilon = 2a/L_z$. This correction term takes into account the finite size of RBCs and results in a finite shear rate at the centerline [27].

D is a model parameter, representing the hydrodynamic diffusivity of RBCs due to hydrodynamic interactions of more than two cells. This effect is relatively weak compared to pair-wise interactions for hematocrits between 10% and 30% [20]. When compared to simulation results, outputs from our existing steady-state theory at $D = 0$ contain 8% relative error in the cell-free layer thickness estimate. This error is reduced to within the tolerance of discretization if D is set to the best-fit values as tabulated in Table III. The best-fit D values increase with hematocrit, which is consistent with its role as a model for higher-order collisions. In the current study of the time-dependent scenario, we set D to the best-fit values and therefore we expect outputs from our theory and simulations to converge to our previously reported steady distributions as $t \to \infty$, regardless of the transient behavior.

Equations similar to Eqs. (1) and (2) have been used in various related studies [28–31] in both simple shear and pressure-driven flows, but our previous work [20] is the only one that explicitly determines the values of u_{lift}, Δ_{CC}, Δ_{PP}, and Δ_{CP} such that we can accurately calculate the corresponding flux contributions. Estimating these parameters from small-scale simulations also vastly reduces the computational work needed as compared to whole blood simulations. The time evolution of particle migration and margination is very briefly mentioned by Rivera *et al.* [31] for an arbitrary magnitude of shear-induced diffusion and lift fluxes. In this study, we solve our governing equations using the same set of inputs as the steady-state study (u_{lift}, Δ_{CC}, Δ_{PP}, Δ_{CP}, and D) and interpret the results on a physical basis.

Equations (1) and (2) are solved numerically using a finite volume scheme. We discretize the channel height domain into $2N + 1$ intervals and advance time with a step size of Δt. We will solve for the values $n_C(z,t)$ and $n_P(z,t)$ at the center of each interval, denoted a_i^k and b_i^k for the concentrations of RBCs and platelets at the center of the ith interval at the kth timestep. The solutions $n_C(z,t)$ and $n_P(z,t)$ are then approximated as piecewise linear functions $n_C(z) = \sum_{j=1}^{N} a_j \xi_j(z)$ and $n_P(z) = \sum_{j=1}^{N} b_j \xi_j(z)$. Using Godunov's method, the finite volume method can be formulated as follows:

$$\frac{\tilde{n}_i^{k+1} - \tilde{n}_i^k}{\Delta z} = -\Delta t\left[\tilde{f}_{i+1/2}^k - \tilde{f}_{i-1/2}^k\right]. \tag{4}$$

$\tilde{n}_i^k$ is the average value of n on the ith interval and can be approximated using the trapezoidal rule in two subintervals: $\tilde{n}_i^k = \frac{1}{8}n_{i-1}^k + \frac{3}{4}n_i^k + \frac{1}{8}n_{i+1}^k$. Therefore, vectors $\tilde{\boldsymbol{n}}_C^k$ and $\tilde{\boldsymbol{n}}_P^k$ can also be expressed in terms of piecewise linear functions using vectors $\boldsymbol{a}^k$ and $\boldsymbol{b}^k$: $\boldsymbol{M}\boldsymbol{a}^k = \tilde{\boldsymbol{n}}_C^k$ and $\boldsymbol{M}\boldsymbol{b}^k = \tilde{\boldsymbol{n}}_P^k$. $\tilde{f}_{i+1/2}^k$ represents the flux at the right boundary of the ith interval and is calculated using the upwind rule:

$$\tilde{f}_{i+1/2}^k = f\left(\tilde{n}_i^k\right) \quad f \geqslant 0 \tag{5}$$

$$= f\left(\tilde{n}_{i+1}^k\right) \quad f < 0. \tag{6}$$

$\tilde{f}(n_i^k)$ is the flux for the ith interval approximated using $\tilde{f}(n_i^k) = \frac{1}{8}f(n_{i-1}^k) + \frac{3}{4}f(n_i^k) + \frac{1}{8}f(n_{i+1}^k)$. To evaluate the integrals F_{CC}, F_{CP}, and F_{PP} in the flux expression, we further divide each interval into five subintervals and use the midpoint rule for integration:

$$F_{AB,i}^k = \sum_{j=1}^{N}\sum_{m=1}^{N} A_i^k B_i^k \int_{\delta_z}\int_{\delta_y}\int_0^{\Delta_{AB}} \xi_j(z_i - b)\xi_m(z_i - b - \delta_z)\delta u \, db \, d\delta_y \, d\delta_z. \tag{7}$$

Equation (4) for the finite volume formulation on each interval can thus be written in the matrix vector form to calculate a_i^k and b_i^k:

$$\boldsymbol{a}^{k+1} = \boldsymbol{a}^k - \frac{\Delta t}{\Delta z}\boldsymbol{M}^{-1}\Delta\tilde{\boldsymbol{f}}_a^k, \tag{8}$$

$$\boldsymbol{b}^{k+1} = \boldsymbol{b}^k - \frac{\Delta t}{\Delta z}\boldsymbol{M}^{-1}\Delta\tilde{\boldsymbol{f}}_b^k. \tag{9}$$

B. Boundary integral simulations

Since few existing simulations have presented the time-dependent migration and margination profiles quantitatively, we perform our own boundary integral simulations of full blood flow to compare with our theory. The simulation method is adopted from Zhao *et al.* [5], and we briefly review the formulation in this section. Our boundary integral simulation consists of three types of equations that determine the RBC membrane velocity u_C, the wall friction force density distribution $[\![\mathbf{f}_W]\!]$, and a double-layer density on platelet surfaces $\boldsymbol{\psi}_P$. The full boundary integral equations for the RBCs and platelets including walls are:

$$\frac{1+\lambda}{2}\mathbf{u}_C - u_\infty = \frac{1-\lambda}{8\pi}\mathbf{K}_{CC}\mathbf{u}_C - \frac{1}{8\pi\mu}\mathbf{N}_{CC}[\![\mathbf{f}_C]\!] - \frac{1}{8\pi}\mathbf{K}_{CP}\boldsymbol{\psi}_P - \frac{1}{8\pi\mu}\mathbf{N}_{CW}[\![\mathbf{f}_W]\!], \tag{10a}$$

$$\begin{aligned}\frac{1}{2}\boldsymbol{\psi}_P - u_\infty = &-\sum_{\beta=1}^{6}(\mathbf{q}^{''\beta},\boldsymbol{\psi}_P)\mathbf{q}^{''\beta} + \frac{1-\lambda}{8\pi}\mathbf{K}_{PC}\mathbf{u}_C \\ &- \frac{1}{8\pi\mu}\mathbf{N}_{PC}[\![\mathbf{f}_C]\!] - \frac{1}{8\pi}\mathbf{K}_{PP}\boldsymbol{\psi}_P - \frac{1}{8\pi\mu}\mathbf{N}_{PW}[\![\mathbf{f}_W]\!],\end{aligned} \tag{10b}$$

$$0 = \frac{1-\lambda}{8\pi}\mathbf{K}_{WC}\mathbf{u}_C - \frac{1}{8\pi\mu}\mathbf{N}_{WC}[\![\mathbf{f}_C]\!] - \frac{1}{8\pi\mu}\mathbf{N}_{WW}[\![\mathbf{f}_W]\!] - \frac{1}{8\pi}\mathbf{K}_{WP}\boldsymbol{\psi}_P, \tag{10c}$$

where u_∞ is the far-field velocity of Poiseuille flow, and $\mathbf{q}^{''\beta}$ are the six independent modes of rigid body motion. The simulation domain spans $0 \leqslant x \leqslant L_x$, $0 \leqslant y \leqslant L_y$, and $0 \leqslant z \leqslant L_z$. We impose periodic boundary conditions in the x and y directions and no-slip boundary conditions on the walls in the z direction. Thus, in the far-field we have Poiseuille flow with a parabolic velocity profile and average flow velocity $\langle u\rangle$: $u^\infty = 6\langle u\rangle\frac{z(L_z-z)}{L_z^2}$. The single- and double-layer kernels $\mathbf{N}$ and $\mathbf{K}$ are defined as

$$(\mathbf{N}[\![f]\!])_j(\mathbf{x}_0) = \int [\![f]\!]_i(\mathbf{x})G_{ij}(\mathbf{x},\mathbf{x}_0)dS(\mathbf{x}), \tag{11}$$

$$(\mathbf{K}\mathbf{u})_j(\mathbf{x}_0) = \int \mathbf{u}_i(\mathbf{x})T_{ijk}(\mathbf{x},\mathbf{x}_0)\mathbf{n}_k(\mathbf{x})dS(\mathbf{x}), \tag{12}$$

and $\mathbf{G}$ and $\mathbf{T}$ are the fundamental Green's function solutions for the Stokeslet and stresslet with periodic boundary conditions [32]. The smooth particle mesh Ewald summation technique [33] is used to accelerate the simulation.

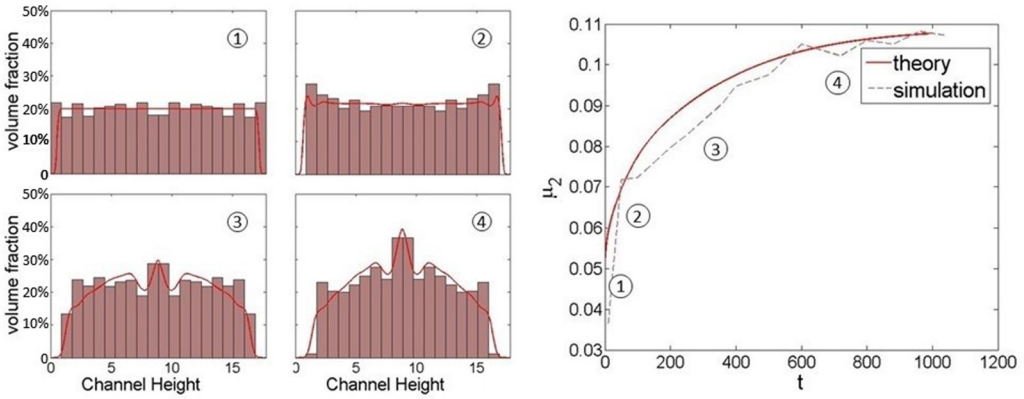

FIG. 2. Comparison between simulation (pink) and theoretical (red) results for RBC concentration distribution $L_z = 17.73$, 20% hematocrit, Ca = 1. (a) Snapshots at different t, where the local volume fraction is defined as $\phi_C(z) = \frac{4\pi}{3}a^3 n_C(z)$. (b) Second moment vs. t. The numbered distribution profiles in (a) match the numbered time periods in (b).

III. RESULTS AND DISCUSSIONS

A. Evolution of margination and migration profile

We first present the time-dependent concentration profiles of RBCs and platelets obtained from both the theory and simulations. The simulation results are averaged over intervals of 5000 time steps. Therefore, our theoretical outputs can achieve a relatively higher spatial resolution because of the fluctuating motion (which is averaged) of the particles in the simulations. As shown in Fig. 2, starting with a uniform concentration distribution, the near-wall region is quickly depleted of RBCs. The concentration at the centerline, however, does not increase immediately after the flow starts. During this short period of time, the concentration profile resembles that of simple shear flow, where the concentration peak is located close to the boundary of the cell-free layer. The concentration profile calculated from the time-dependent theory eventually approaches that of the steady-state theory, which is determined independently by Newton's iteration using a uniform concentration profile as an initial guess [20]. Thus, we have also verified the steady-state theory as previously reported [20]. The total time for RBC migration to reach steady state is set by the time for development of the center peak concentration. The migration behavior we observe is as expected because both the lifting force and the shear-induced diffusion are strongest near the wall and decay at the center due to the vanishing shear rate. To quantitatively examine the migration phenomena, we plot the second moment of the concentration profile defined as: $\mu_2 = \int_0^{L_z}(z - \frac{L_z}{2})^2\,(\bar{n} - n(z))dz$. We demonstrate good agreement between theory and simulations (within 10% relative error) throughout the time evolution. The convergence of the steady-state profile as $t \to \infty$ is a prerequisite for the accuracy in the time-dependent result.

The transient behavior that we observe in pressure-driven flow is, however, not the same as in the simple shear flow case, primarily because, in the latter instance, the shear-induced diffusion remains strong away from the wall throughout the channel [20]. At steady state, the cell-free layer thicknesses differ by up to 20% in simple shear and pressure-driven flow at matching characteristic shear rate [20]. Therefore, a simple shear approximation underestimates the time to reach steady state as demonstrated in Fig. 3.

We use a criteria of 95% quantile to calculate the time to form a cell-free layer t_{CFL} and reach steady state $t_{\mathrm{SS},C}$. For the case of 20% hematocrit and $L_z = 17.73$ (50 μm), the dimensionless t_{CFL} is roughly 290, and agrees with Katanov and coworkers' [10] empirical estimation of 200 for a cylindrical tube at matching characteristic shear rate. However, as far as we are aware, no estimates are presently available for the overall timescale $t_{\mathrm{SS},C}$.

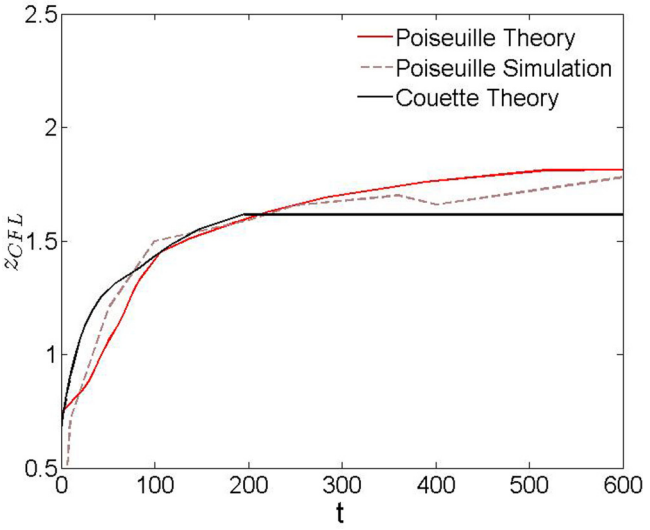

FIG. 3. Comparison of the cell-free layer thickness vs. t; error bar represents discretization error, $L_z = 17.73$, 20% hematocrit, Ca $= 1$.

We next examine the evolution of platelet margination. As shown in Fig. 4, starting with a uniform distribution, a concentration peak near each wall develops shortly after the onset of flow. These peaks in platelet concentration are located closer to the wall than the RBC concentration peaks and thus they are "inside" the cell-free layers. To reach the final steady state, platelets undergo a slow margination, characterized by the depletion of platelets from the bulk region. In Fig. 4, we plot the second moment of platelet concentration. As is clearly seen around position "2" in the time trace, a slowing in the rate of variation of the second moment is observed for a short time period, which coincides with the cell-free layer formation timescale. To further investigate whether this short period of relative stagnation in the evolution of platelet concentration is related to RBC migration, we again calculate the platelet evolution from our theory but this time with the RBC initial configuration set to its

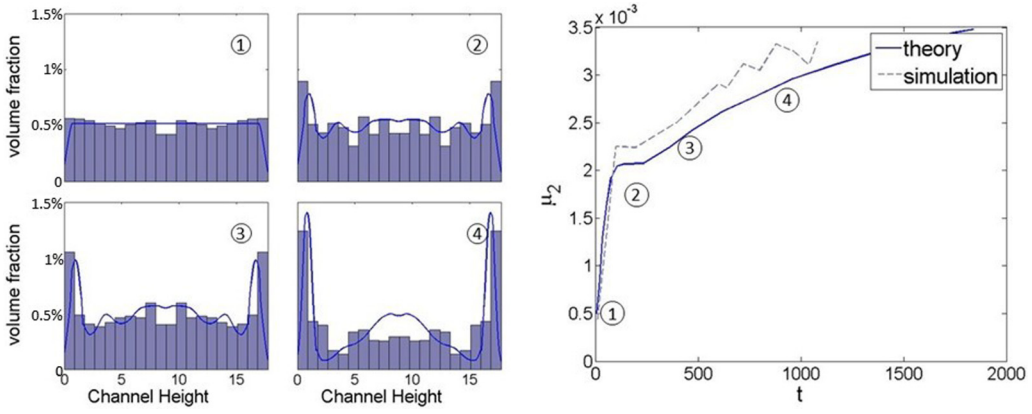

FIG. 4. Comparison between simulation (purple) and theoretical (blue) results for platelet concentration distribution $L_z = 17.73$, 20% hematocrit, Ca $= 1$. (a) Snapshots at different t, where the local volume fraction is defined as $\phi_P(z) = \frac{4\pi}{3} a_P^3 n_P(z)$. (b) Second moment vs. t. The numbered distribution profiles in (a) match the numbered time periods in (b).

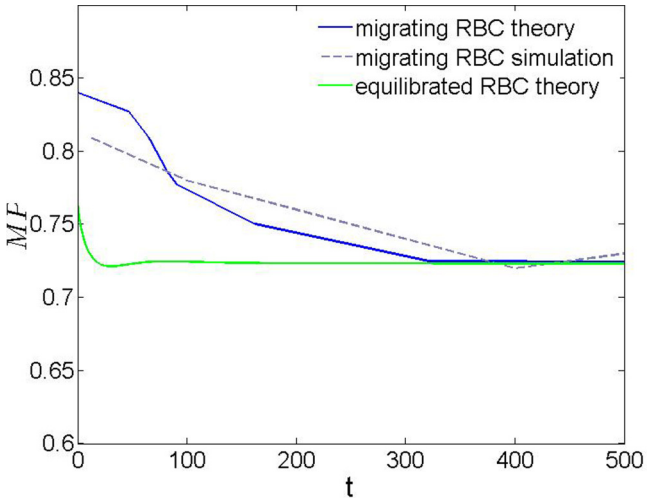

FIG. 5. Comparison of margination parameter vs. t. The initial RBC concentration is uniform (blue, purple) and has formed a cell-free layer (green), $L_z = 17.73$, 20% hematocrit, Ca = 1.

configuration at $t = t_{\mathrm{CFL}}$, i.e., just after the cell-free layer has formed. The resulting evolution of the platelet concentration profile no longer has a stagnation period, and reaches steady state significantly more quickly. The final concentration distribution profile at steady state, however, remains unchanged. The dependence of platelet margination on the initial RBC distribution proves that the fast initial margination is closely related to the formation of the cell-free layer and our findings are thus similar to the prediction by Crowl and coworkers [19]. We denote this timescale as t_{FM}. This timescale can be further quantified using a margination parameter $\mathrm{MP} = \frac{\int_0^{z_{\mathrm{CFL}}}(z-L_z/2)^2 n(z)dz}{(L_z/2)^2\int_0^{z_{\mathrm{CFL}}} n(z)dz}$, which represents the degree of margination inside the cell-free layer. We plot MP vs. time in Fig. 5. t_{FM} is thus calculated as the time that the difference between MP(t_{FM}) and the steady-state MP value is within 5%.

The overall timescale to reach a complete steady state platelet distribution, $t_{\mathrm{SS},P}$, is the longest timescale among the four timescales we have investigated: $t_{\mathrm{SS},C}$, $t_{\mathrm{SS},P}$, t_{CFL}, and t_{FM}. The separation of the aforementioned two timescales for platelet margination also agrees with the observations of both Vahidkhah *et. al.* [8] and Zhao *et. al.* [5] who noted that platelet margination in the bulk region due to platelet-RBC interactions is a slow process while the time to cross the cell-free layer is a fast process due to the sharp concentration gradient. While the two aforementioned groups examined the trajectories of individual platelets, we use our theory to arrive at the same conclusion by looking at the overall behavior of the blood suspension.

B. Effects of channel height, hematocrit, and capillary number

To further examine the governing mechanisms for migration and margination, we vary the channel height L_z, shear rate and hematocrit. The effects of channel height and hematocrit on RBC migration are shown in Fig. 6. The cell-free layer thickness increases weakly with the channel height [10], and therefore t_{CFL} increases for wider channels. In the cell-laden region, the lift velocity drops significantly and therefore it is the RBC-RBC interactions that influence the rate of cross-flow transport. The length scale for this bulk region increases with channel height, despite the slight increase in cell-free layer thickness. The overall timescale $t_{\mathrm{SS},C}$ thus also increases with channel height.

The hematocrit is another key parameter influencing the time-dependent behavior. Examining Fig. 6, we find that the migration profile at steady state changes with hematocrit and this includes an increase in the second moment of the RBC distribution. The steady distribution is also reached significantly faster at higher hematocrits. This is as expected since both the lift and the shear-

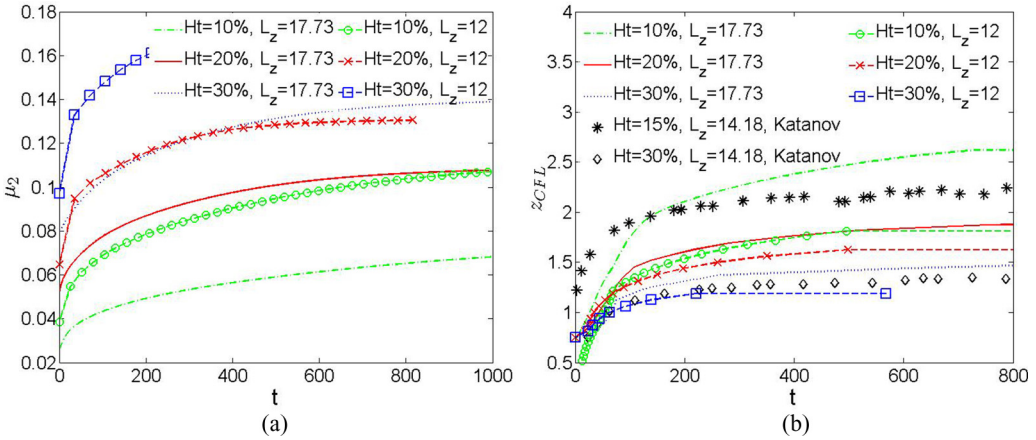

FIG. 6. Comparison of RBC migration at different channel heights and hematocrits (Ht). (a) Second moment of concentration distribution vs. t. (b) Cell-free layer thickness vs. t compared with simulation results by Katanov *et al.* [10].

induced diffusional fluxes increase with hematocrit. Therefore, the rate of migration increases with increasing hematocrit. Our predictions for the cell-free layer thickness also agree nearly quantitatively with simulation results by Katanov and co-workers [10]. Although their simulations are done in cylindrical channels, we observe very similar trends with hematocrit and channel height at matching characteristic shear rates.

Unlike the hematocrit and channel height, the capillary number does not play a significant role in the rate of RBC migration as shown in Fig. 7. Both μ_2 for the overall concentration distribution and the cell-free layer thickness seem to converge for $\mathrm{Ca} > 0.5$. As Zhao *et al.* [5] pointed out, $\mathrm{Ca} = 0.5$ represents the onset of RBC tank-treading behavior. Thus, the RBC shape remains unchanged at higher values of Ca. A further increase in shear rate has therefore similar effects on both the lift and shear-induced diffusion—i.e., the corresponding fluxes increase proportionally to the shear rate. In our study, we focus on capillary numbers ranging between 0.25 and 2, which match the physiological flow regime. A wider range of capillary numbers was examined by Katanov *et al.* [10]. They observed that the steady-state cell-free layer thickness first increases with the flow shear rate and saturates at shear rates greater than 1000 s^{-1}, again in agreement with our comments above.

The effects of channel height and hematocrit on platelet margination are summarized in Fig. 8. Similar to the cell-free layer thickness, the steady-state value of MP shows a monotonic variation with

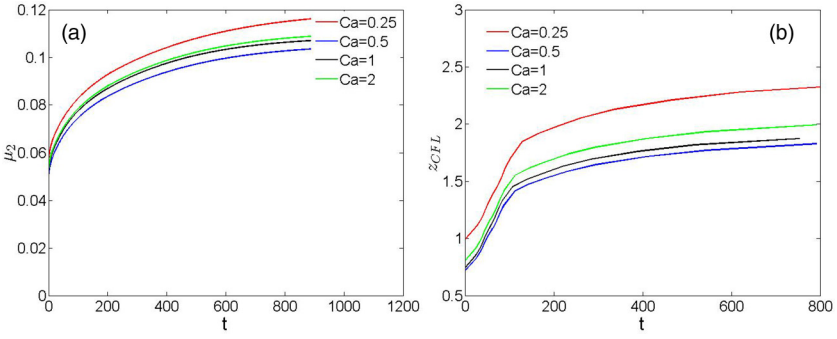

FIG. 7. Comparison of RBC migration at different capillary numbers. (a) Second moment of concentration distribution vs. t. (b) Cell-free layer thickness vs. t, $L_z = 17.73$, 20% hematocrit.

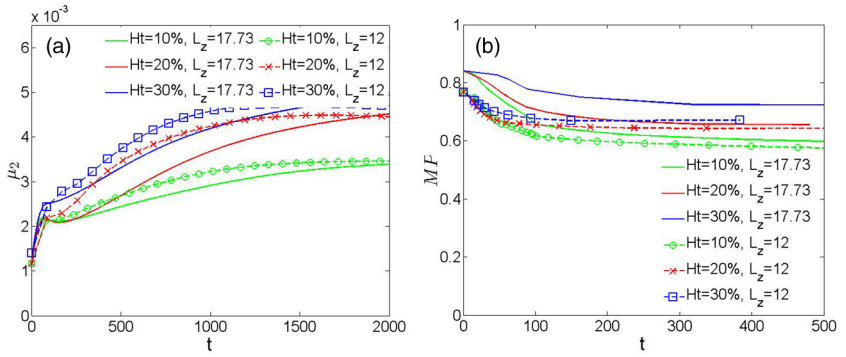

FIG. 8. Comparison of platelet margination at different channel heights and hematocrits (Ht). (a) Second moment of concentration distribution vs. t. (b) Margination parameter vs. t.

respect to increasing hematocrit. At lower hematocrit, platelets are less concentrated near the wall and are more evenly spread over a wider cell-free layer. Therefore, the μ_2 value is smaller. When the channel height increases, the cell-free layer thickness becomes smaller relative to the channel height. Therefore, platelets are more marginated and have a higher μ_2 value. Both the overall timescale and the fast margination timescale always decrease with the hematocrit, since the frequency of RBC-platelet interactions is proportional to the RBC concentration. An increase in channel height again increases both margination timescales, as in the case of RBC migration, because the initially evenly-distributed platelets need to travel a longer distance to reach the cell-free layer and fully marginate.

The effects of the capillary number on platelet margination are shown in Fig. 9. Since RBC migration essentially controls platelet margination and is nearly independent of the capillary number, we see a very modest effect of capillary number on the platelet margination parameter.

C. Scaling analysis

So far we have presented a qualitative discussion of the factors that influence RBC migration. We turn now to a discussion of our results such that these factors can be interpreted in a more quantitative manner. In this context, we first perform a scaling analysis for the four different timescales using the following approximate formulas, based on the identified governing mechanisms for each transport

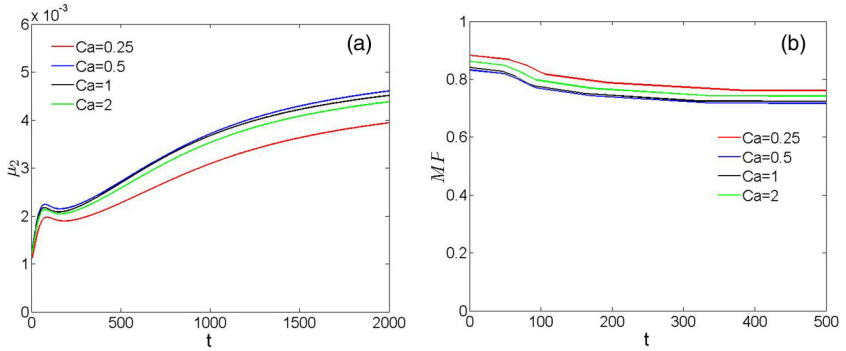

FIG. 9. Comparison of platelet margination at different capillary numbers. (a) Second moment of concentration distribution vs. t. (b) Margination parameter vs. t, $L_z = 17.73$, 20% hematocrit.

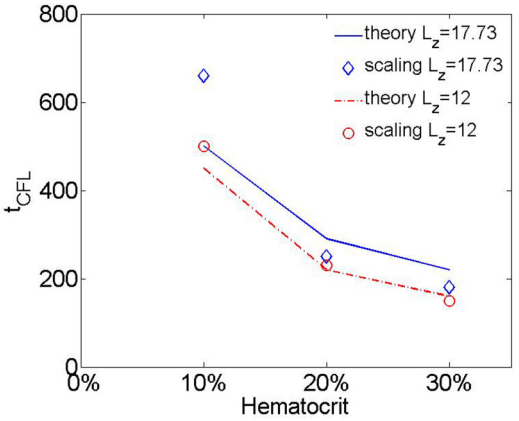

FIG. 10. Comparison between theory and scaling for the time to form a cell-free layer t_{CFL}.

process:

$$t_{\mathrm{CFL}} = \int_0^{z_{\mathrm{CFL}}} \frac{dz}{u_{\mathrm{lift}}}, \tag{13}$$

$$t_{\mathrm{SS},C} = \frac{\left(\frac{L_z - 2z_{\mathrm{CFL}}}{4}\right)^2}{D_{\mathrm{cell}}} + t_{\mathrm{CFL}}, \tag{14}$$

$$t_{\mathrm{FM}} = \int_0^{z_{\mathrm{CFL}}} \frac{dz}{u_{\mathrm{platelet}}}, \tag{15}$$

$$t_{\mathrm{SS},P} = \frac{\left(\frac{L_z - 2z_{\mathrm{CFL}}}{4}\right)^2}{D_{\mathrm{platelet}}} + t_{\mathrm{FM}}. \tag{16}$$

We obtain the parameters in these equations through various sources. First, the hydrodynamic diffusivity of RBCs D_{cell} and platelets D_{platelet} are directly obtained from previously published research [5,18,19,34]. u_{platelet} is a drift velocity of platelets into the clear fluid layer caused by the difference in the rates of platelet-RBC collisions, plus platelet-platelet collisions, between the bulk suspension and the cell-free layer. Therefore, it is difficult for marginated platelets to re-enter the cell-laden region [35]. Since there are very few literature sources which quantify this effect [19], we calculate u_{platelet} indirectly based on the difference in diffusivity D_{platelet} inside and outside the cell-free layer: $u_{\mathrm{platelet}} = \Delta D_{\mathrm{platelet}}/z_{\mathrm{CFL}}$ [34]. Because the RBCs are characterized by a plethora of highly deformable shapes in pressure-driven flow, the rheology of blood in this flow is much more complex than that of a suspension of nearly spherical particles. Therefore, we do not expect the scaling analysis and our theory to be in quantitative agreement. However, the estimates based on the scaling analysis should capture the important trends in timescale variation and reveal the fundamental physics associated with the different controlling transport mechanisms.

As can be seen from Fig. 10, the convective timescale for RBCs based on Eq. (13) agrees reasonably well with the result as determined from the Boltzmann collision theory in Eq. (1). Therefore, the increase of t_{CFL} with both hematocrit and channel height can be explained simply by the change in the cell-free layer thickness. Note that a more significant discrepancy between scaling and theory is observed for lower hematocrit and wider channels, both of which produce thicker cell-free layers. In this case, the lift velocity decays significantly near the edge of the cell-free layer and, thus shear-induced diffusion, i.e., RBC-RBC interactions, which are not included in the scaling analysis in Eq. (13), may play a bigger role.

Equation (14) approximates the overall migration timescale by simply adding the time associated with lift inside the cell-free layer plus the time for shear-induced diffusion across the bulk region. As

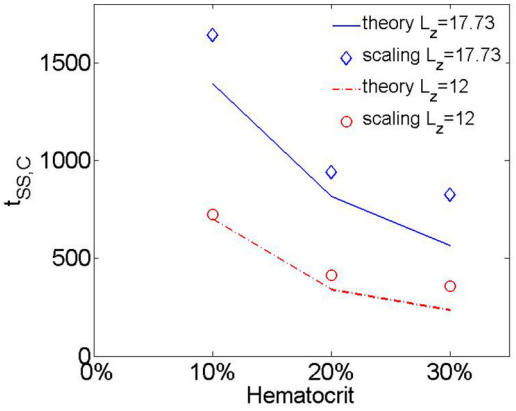

FIG. 11. Comparison between theory and scaling for RBC migration $t_{SS,C}$. D_{cell} is referenced from Crowl and Fogelson [19].

shown in Fig. 11, while both the theory and scaling report $t_{SS,C}$ values that decrease with hematocrit and channel height, the change due to hematocrit is less significant in the scaling analysis. In Crowl and Fogelson's estimation of D_{cell} (which we have used in making this scaling determination), its value changes only weakly when the hematocrit increases from 20% to 40%, in contrast to an approximately linear increase if only two-body interactions were important. Therefore, it is no surprise that the scaling estimate for migration in the bulk region deviates from our Boltzmann theory, the latter of which determines F_{CC} based on the product of two particle interactions.

The scaling t_{FM} is presented in Fig. 12. The scaling argument overpredicts the value of t_{FM}, although a similar qualitative trend with increasing hematocrit is demonstrated. Thus, the platelet drift velocity is likely to be underpredicted by our approximation or even the present literature that we have referenced [19]. As mentioned previously, the indirect calculation of the drift velocity accounts for the variation of diffusivity over the length scale of the cell-free layer. Platelet diffusivity is mainly due to RBC-platelet interactions. However, given the fact that platelet drift results from the sharp concentration gradient of RBCs at the edge of the cell-free layer, the actual variation of platelet diffusivity occurs on a very small length scale, e.g., the size of a RBC. Thus, we expect, simply on this basis, that the actual platelet drift velocity will be somewhat greater than the approximation used in our scaling analysis.

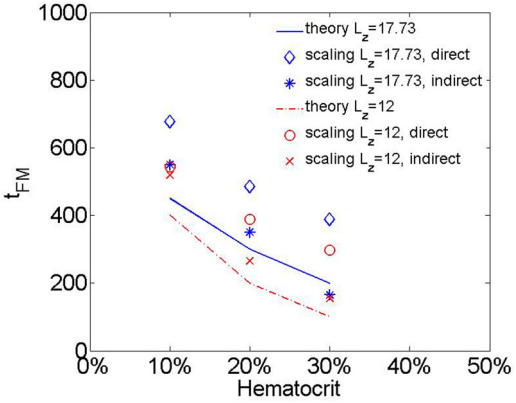

FIG. 12. Comparison between theory and scaling for platelet fast margination t_{FM} with drift velocity from direct [19] and indirect estimations [34].

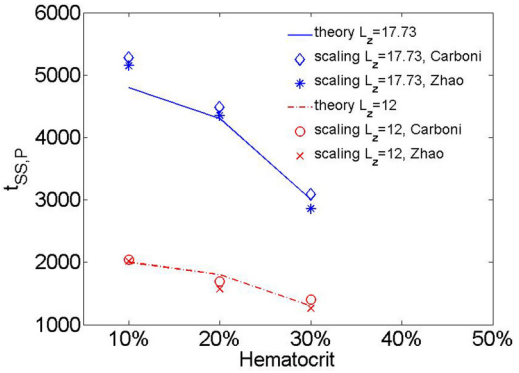

FIG. 13. Comparison between theory and scaling for platelet full margination $t_{SS,P}$. D_{platelet} is referenced from Carboni *et al.* [18] and Zhao *et al.* [5].

Despite the discrepancy in the estimation of t_{FM}, the scaling analysis and the theory agree well for the overall margination timescale $t_{SS,P}$ as shown in Fig. 13. As we have discussed previously, RBC-platelet interactions in the bulk region result in shear-induced diffusion, which is a slow process as compared to the platelets exiting the bulk region and entering the cell-free layer. $t_{SS,P}$ is thus dominated by the $\frac{(\frac{L_z-2z_{\text{CFL}}}{4})^2}{D_{\text{platelet}}}$ term in Eq. (15) as evidenced by a comparison between Figs. 11 and 12. The relatively small size of platelets as compared to RBCs makes it easier to measure their diffusivity. Thus the abundance of literature values which are in reasonable agreement for D_{platelet} makes the scaling analysis more reliable.

D. Axial variation and entrance lengths

We now briefly consider the entrance length problem by introducing axial variation of the concentration profile at steady state. For simplicity, we will only study the entrance length of RBC migration, with the following governing equation:

$$\frac{u_x \partial n_C}{\partial x} + \frac{\partial (u_{lift} n_C)}{\partial z} + \frac{\partial F_{CC}}{\partial z} - \frac{\partial}{\partial z}\left(D \frac{\partial n_C}{\partial z}\right) = 0. \tag{17}$$

With all other terms unchanged from the time-dependent problem in Eq. (17), we assume a parabolic flow profile for u_x: $u_x = 6\langle u \rangle \frac{z(L_z - z)}{L_z^2}$, and thus ignore the "pluglike" velocity profile due to the nonuniform distribution of RBCs [5]. Similar problems have been considered for the migration of rigid spheres [27], and a marching method was chosen to facilitate the calculation of the steady-state concentration profile. We adopt this same marching method and the numerical implementation is briefly summarized in Eqs. (18) and (19), viz:

$$\begin{aligned} &\frac{u_x[n_C(x) - n_C(x - \Delta x)]}{\Delta x} + \frac{1}{2}\left[\frac{\partial (u_{\text{lift}} n_C)}{\partial z} + \frac{\partial F_{CC}}{\partial z} - \frac{\partial}{\partial z}\left(D \frac{\partial n_C}{\partial z}\right)\right]_{x-\Delta x} \\ &+ \frac{1}{2}\left[\frac{\partial (u_{\text{lift}} n_C)}{\partial z} + \frac{\partial F_{CC}}{\partial z} - \frac{\partial}{\partial z}\left(D \frac{\partial n_C}{\partial z}\right)\right]_{x} = 0, \end{aligned} \tag{18}$$

$$\frac{\tilde{n}_{i,j}^{k+1} - \tilde{n}_{i,j}^{k}}{\Delta z} = -\Delta t\left[\tilde{f}_{i+1/2,j}^{k} - \tilde{f}_{i-1/2,j}^{k}\right]. \tag{19}$$

In addition to discretization in z, we discretize the x domain with Δx using an Euler method as shown in Eq. (18). The finite volume formulation in z domain of Eq. (19) is similar to Eq. (4) for the ith interval in z and jth interval in x. The right-hand side of Eq. (19) is now modified according to

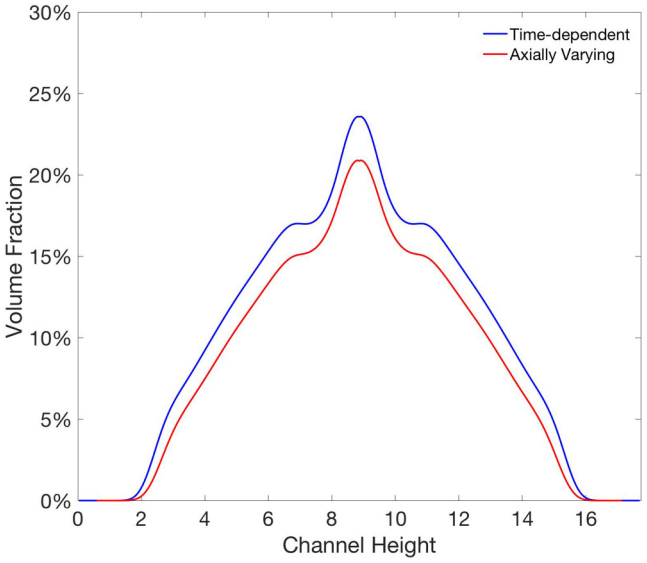

FIG. 14. Comparison between the steady-state RBC concentration profile from time-dependent problem and the axial variation problem.

Eq. (18). Starting from a uniform concentration profile at $x = 0$, we march one step downstream to $x = \Delta x$, and advance time until $n_C(\Delta x, z)$ reaches steady state, i.e., μ_2 of the concentration profile changes by no more than 10^{-6}. This marching process is repeated until no axial variation is observed, and the computational domain in x is at least 100 times the channel height in z.

The steady-state RBC concentration profiles for the time-dependent problem and the fully-developed axial variation problem are compared in Fig. 14. Both problems predict similar shapes of the RBC concentration profile. One noticeable distinction is the reduction of hematocrit for the axial variation problem, which is due to the varying RBC velocity in the x direction. As one moves down the channel, RBCs are more concentrated near the center, and therefore have a higher average velocity than $\langle u \rangle$. The hematocrit specified at the inlet is thus lower than the hematocrit collected at the outlet, leading to a reduction of hematocrit inside the channel. This reduction of hematocrit is commonly referred to as the Fahraeus effect, and an emprical correlation is given as: $\frac{\mathrm{Ht,out}}{\mathrm{Ht,in}} = \mathrm{Ht,in} + (1 - \mathrm{Ht,in})[1 + 1.7\exp(-0.415L_z) - 0.6\exp(-0.011L_z)]$ (L_z in microns) [36]. The reduction of hematocrit is tabulated in Table IV for various channel heights and inlet hematocrits. We predict a maximum reduction of 4% hematocrit over the conditions studied.

Using a 95% quantile as we did for the time-dependent problem, we calculate entrance lengths (i.e., lengths to achieve a fully developed profile) for both the cell-free layer formation and complete

TABLE IV. Comparison of inlet and outlet hematocrits for various channel heights. Ca = 1 for the axially varying problem. Flow conditions for the empirical correlation [36] are unknown.

L_z	Ht,in	Ht,out	Ht,out empirical
12	10%	8.0%	5.9%
12	20%	17.1%	12.6%
12	30%	26.2%	20.3%
17.73	10%	8.6%	6.3%
17.73	20%	17.5%	13.5%
17.73	30%	27%	21.5%

TABLE V. Comparison of entrance lengths with those estimated from time-dependent problems, in mm, Ca = 1.

L_z	Ht,in	CFL entrance length	$t_{\mathrm{CFL}}\langle u\rangle$	SS entrance length	$t_{\mathrm{SS},C}\langle u\rangle$
12	10%	2.54	2.54	5.9	3.95
12	20%	1.14	1.25	1.4	1.92
12	30%	0.76	0.90	0.97	1.32
17.73	10%	10.62	4.17	14.37	11.60
17.73	20%	3.75	2.42	6.75	6.80
17.73	30%	1.87	1.83	5.06	4.70

migration. Using the time-dependent problem, the entrance length is typically approximated as the time to steady state multiplied by the average velocity $\langle u\rangle$ [10]. The comparison between the actual entrance length and this approximation is shown in Table V, and they are clearly of similar magnitude. Therefore, the time-dependent estimate provides a reasonable estimate of the real entrance length problem according to our model. In the case of platelet margination, $t_{\mathrm{SS},P}\langle u\rangle = 3.5$ cm for 20% hematocrit and $L_z = 17.73$ (50 μm), which agrees with Fitzgibbon *et al.*'s [4] O(1 cm) experimental estimation. We expect all entrance lengths will be nearly independent of the capillary number, for Ca > 0.5, based on our previous work [20].

IV. CONCLUSIONS

We have extended our existing coarse-grained theory for RBC migration and platelet margination to consider the time dependence in these two phenomena. We discovered two disparate timescales associated with each type of cross-flow motions. The separation of timescales is associated with different governing mechanisms inside and outside the cell-free layer. Inside the cell-free layer, i.e., in the very near-wall region, RBCs experience a strong lift force away from the wall that results in a convective motion that ultimately creates the cell-free layer. Outside the cell-free layer, however, the lifting force decays dramatically and the RBC-RBC interactions (i.e., hydrodynamic "collisions") play the primary transport role. Due to the reduction of shear rate (and thus lift) outside the cell-free layer, a second, longer timescale is necessary for establishing the final steady-state RBC concentration distribution based on the aforementioned collision processes.

Platelet margination is governed by RBC-platelet interactions overall and complemented by platelet-platelet interactions inside the cell-free layer. Therefore, the associated transport timescales are directly associated with RBC dynamics. The edge of the cell-free layer creates a drift force, which drives the platelets into the cell-free layer from the bulk region. Initially, as the cell-free layer is being developed, platelets in the vicinity of the receding "edge" of RBCs quickly enter the cell-free layer and this process results in "fast margination." On the other hand, platelets that are in the bulk suspension and hence away from the wall undergo a slow process of marginating to the wall via shear-induced diffusion due to RBC-platelet interactions.

Our theory provides insights into the time evolution of migration and margination that is rarely discussed, and is verified against whole blood simulations. We elucidate the connection between the axially varying "entrance length" problem and the time-dependent problem, and demonstrate how entrance lengths can be approximated from the relevant timescales associated with the latter theory. It is possible to apply our theory to other types of rigid particles with varying shapes and sizes, as long as the input parameters are available based on experimental measurements or results from small-scale simulations. Furthermore, the scaling analysis indicates that quantities which are difficult to measure from simulations and experiments, such as the platelet drift velocity, may be easily obtained from our theory with relatively good accuracy.

ACKNOWLEDGMENTS

The authors acknowledge support from the US Army High Performance Computing Research Center (AHPCRC) and support from Stanford University's Certainty computer cluster that is funded by the American Recovery and Reinvestment Act (ARRA) of 2009 (Grant No. W911NF07200271). Q.M.Q. is supported by Stanford Graduate Fellows in Science and Engineering (SGF).

[1] P. A. Aarts, S. A. van den Broek, G. W. Prins, G. D. Kuiken, J. J. Sixma, and R. M. Heethaar, Blood platelets are concentrated near the wall and red blood cells, in the center in flowing blood, Arteriosclerosis **8**, 819 (1988).

[2] R. Fahreus and T. Lindqvist, The viscosity of the blood in narrow capillary tubes, Am. J. Physiol. **96**, 562 (1931).

[3] G. J. Tangelder, H. C. Teirlinck, D. W. Slaaf, and R. S. Reneman, Distribution of blood platelets flowing in arterioles, Am. J. Physiol. **248**, H318 (1985).

[4] S. Fitzgibbon, A. P. Spann, Q. M. Qi, and E. S. G. Shaqfeh, In-vitro measurement of particle margination in the microchannel flow: Effect of varying hematocrit, Biophys. J. **108**, 2601 (2015).

[5] H. Zhao, E. S. G. Shaqfeh, and V. Narsimhan, Shear-induced particle migration and margination in a cellular suspension, Phys. Fluids **24**, 011902 (2012).

[6] A. Kumar and M. D. Graham, Margination and segregation in confined flows of blood and other multicomponent suspensions, Soft Matter **8**, 10536 (2012).

[7] J. B. Freund and B. Shapiro, Transport of particles by magnetic forces and cellular blood flow in a model microvessel, Phys. Fluids **24**, 051904 (2012).

[8] K. Vahidkhah and P. Bagchi, Microparticle shape effects on margination, near-wall dynamics and adhesion in a three-dimensional simulation of red blood cell suspension, Soft Matter **11**, 2097 (2015).

[9] I. Pivkin, P. Richardson, and G. Karniadakis, *Effect of Red Blood Cells on Platelet Aggregation* (Institute of Electrical and Electronics Engineers, Piscataway, NJ, 2009).

[10] D. Katanov, G. Gompper, and D. A. Fedosov, Microvascular blood flow resistance: Role of red blood cell migration and dispersion, Microvasc. Res. **99**, 57 (2015).

[11] C. R. Valeri, G. Cassidy, L. E. Pivacek, G. Ragno, W. Lieberthal, J. P. Crowley, S. F. Khuri, and J. Loscalzo, Anemia-induced increase in the bleeding time: Implications for treatment of nonsurgical blood loss, Transfusion **41**, 977 (2001).

[12] M. Mehrabadi, Effects of red blood cells and shear rate on thrombus growth, Doctoral dissertation, Georgia Institute of Technology, 2014.

[13] K. Müller, D. A. Fedosov, and G. Gompper, Margination of micro- and nano-particles in blood flow and its effect on drug delivery, Sci. Rep. **4**, 4871 (2014).

[14] R. D'Apolito, G. Tomaiuolo, F. Taraballi, S. Minardi, D. Kirui, X. Liu, A. Cevenini, R. Palomba, M. Ferrari, F. Salvatore *et al.*, Red blood cells affect the margination of microparticles in synthetic microcapillaries and intravital microcirculation as a function of their size and shape, J. Controlled Release **217**, 263 (2015).

[15] H. W. Hou, L. Wu, D. P. Amador-Munoz, M. P. Vera, A. Coronata, J. A. Englert, B. D. Levy, R. M. Baron, and J. Han, Broad spectrum immunomodulation using biomimetic blood cell margination for sepsis therapy, Lab Chip **16**, 688 (2016).

[16] J. Tan, S. Shah, A. Thomas, H. D. Ou-Yang, and Y. Liu, The influence of size, shape and vessel geometry on nanoparticle distribution, Microfluid. Nanofluid. **14**, 77 (2013).

[17] A. S. Popel and P. C. Johnson, Microcirculation and hemorheology, Annu. Rev. Fluid Mech. **37**, 43 (2005).

[18] E. J. Carboni, B. H. Bognet, G. M. Bouchillon, A. L. Kadilak, L. M. Shor, M. D. Ward, and A. W. K. Ma, Direct tracking of particles and quantification of margination in blood flow, Biophys. J. **111**, 1487 (2016).

[19] L. Crowl and A. L. Fogelson, Analysis of mechanisms for platelet near-wall excess under arterial blood flow conditions, J. Fluid Mech. **676**, 348 (2011).

[20] Q. M. Qi and E. S. G. Shaqfeh, Theory to predict particle migration and margination in the pressure-driven channel flow of blood, Phys. Rev. Fluids **2**, 093102 (2017).
[21] K. Sinha and M. D. Graham, Dynamics of a single red blood cell in simple shear flow, Phys. Rev. E **92**, 042710 (2015).
[22] L. Lanotte, J. Mauer, S. Mendez, D. A. Fedosov, J. Fromental, V. Claveria, F. Nicoud, G. Gompper, and M. Abkarian, Red cells' dynamic morphologies govern blood shear thinning under microcirculatory flow conditions, Proc. Natl. Acad. Sci. USA **113**, 13289 (2016).
[23] R. Skalak, N. Ozkaya, and T. C. Skalak, Biofluid mechanics, Annu. Rev. Fluid Mech. **21**, 167 (1989).
[24] H. H. Lipowsky, S. Kovalcheck, and B. W. Zweifach, The distribution of blood rheological parameters in the microvasculature of cat mesentery, Circ. Res. **43**, 738 (1978).
[25] G. Coupier, B. Kaoui, T. Podgorski, and C. Misbah, Noninertial lateral migration of vesicles in bounded poiseuille flow, Phys. Fluids **20**, 111702 (2008).
[26] M. Marchioro and A. Acrivos, Shear-induced particle diffusivities from numerical simulations, J. Fluid Mech. **443**, 101 (2001).
[27] R. M. Miller and J. F. Morris, Normal stress-driven migration and axial development in pressure-driven flow of concentrated suspensions, J. Non-Newtonian Fluid Mech. **135**, 149 (2006).
[28] K. Sinha and M. D. Graham, Shape-mediated margination and demargination in flowing multicomponent suspensions of deformable capsules, Soft Matter **12**, 1683 (2016).
[29] V. Narsimhan, H. Zhao, and E. S. G. Shaqfeh, Coarse-grained theory to predict the concentration distribution of red blood cells in wall-bounded Couette flow at zero Reynolds number, Phys. Fluids **25**, 061901 (2013).
[30] M. Zurita-Gotor, J. Bławzdziewicz, and E. Wajnryb, Layering Instability in a Confined Suspension Flow, Phys. Rev. Lett. **108**, 068301 (2012).
[31] R. G. Henriquez Rivera, X. Zhang, and M. D. Graham, Mechanistic theory of margination and flow-induced segregation in confined multicomponent suspensions: Simple shear and poiseuille flows, Phys. Rev. Fluids **1**, 060501 (2016).
[32] H. Hasimoto, On the periodic fundamental solutions of the Stokes equations and their application to viscous flow past a cubic array of spheres, J. Fluid Mech. **5**, 317 (1959).
[33] D. Saintillan, E. Darve, and E. S. G. Shaqfeh, A smooth particle-mesh Ewald algorithm for stokes suspension simulations: The sedimentation of fibers, Phys. Fluids **17**, 033301 (2005).
[34] K. Vahidkhah, S. L. Diamond, and P. Bagchi, Platelet dynamics in three-dimensional simulation of whole blood, Biophys. J. **106**, 2529 (2014).
[35] A. A. Tokarev, A. A. Butylin, and F. I. Ataullakhanov, Platelet adhesion from shear blood flow is controlled by near-wall rebounding collisions with erythrocytes, Biophys. J. **100**, 799 (2011).
[36] A. R. Pries, T. W. Secomb, P. Gaehtgens, and J. F. Gross, Blood flow in microvascular networks. Experiments and simulation, Circ. Res. **67**, 826 (1990).